1 **Truncated RNA-binding protein production by DUX4-induced systemic inhibition of**

2 **nonsense-mediated RNA decay**

3

4 Amy E. Campbell[1*], Michael C. Dyle[1*], Lorenzo Calviello[2*], Tyler Matheny[3], Kavitha

5 Sudheendran[4], Michael A. Cortazar[1], Thomas Forman[5,6], Rui Fu[3], Austin E. Gillen[3], Marvin H.

6 Caruthers[4], Stephen N. Floor[7,8], and Sujatha Jagannathan[1,3†]

7

8 [1]Department of Biochemistry and Molecular Genetics, University of Colorado Anschutz Medical

9 Campus, Aurora, CO 80045, USA.

10 [2]Human Technopole, Milan, Italy.

11 [3]RNA Bioscience Initiative, University of Colorado Anschutz Medical Campus, Aurora, CO

12 80045, USA.

13 [4]Department of Biochemistry, University of Colorado Boulder, Boulder, CO 80309, USA.

14 [5]Department of Craniofacial Biology, University of Colorado Anschutz Medical Campus, Aurora,

15 CO 80045, USA.

16 [6]Medical Scientist Training Program, University of Colorado Anschutz Medical Campus, Aurora,

17 CO 80045, USA.

18 [7]Department of Cell and Tissue Biology, University of California, San Francisco, San Francisco,

19 CA 94143, USA.

20 [8]Helen Diller Family Comprehensive Cancer Center, University of California, San Francisco,

21 San Francisco, CA 94143, USA.

22

23 *These authors contributed equally

24 †Correspondence: sujatha.jagannathan@cuanschutz.edu

25

26 Running title: NMD inhibition induces truncated proteins

27 Keywords: NMD, DUX4, FSHD, translation, splicing

28   **ABSTRACT**

29   Nonsense-mediated RNA decay (NMD) is a surveillance mechanism that degrades both

30   canonical and aberrant transcripts carrying premature translation termination codons. NMD is

31   thought to have evolved to prevent the synthesis of toxic truncated proteins. However, whether

32   global inhibition of NMD results in widespread production of truncated proteins is unknown. A

33   human genetic disease, facioscapulohumeral muscular dystrophy (FSHD) features acute

34   inhibition of NMD upon expression of the disease-causing transcription factor, DUX4. Here,

35   using a cell-based model of FSHD, we show the production of hundreds of truncated proteins

36   from physiological NMD targets. Using ribosome profiling, we map the precise C-terminal end of

37   these aberrant truncated proteins and find that RNA-binding proteins are especially enriched for

38   aberrant truncations. The stabilized NMD isoform of one RNA-binding protein, SRSF3, is

39   robustly translated to produce a stable truncated protein, which can also be detected in FSHD

40   patient-derived myotubes. Notably, ectopic expression of truncated SRSF3 alone confers

41   toxicity and its downregulation is cytoprotective. Our results demonstrate the genome-scale

42   impact of NMD inhibition. This widespread production of potentially deleterious truncated

43   proteins has implications for FSHD biology as well as other genetic diseases where NMD is

44   therapeutically modulated.

INTRODUCTION

Nonsense-mediated RNA decay (NMD) degrades transcripts containing premature termination codons (PTCs) that arise from nonsense mutations or RNA processing errors. Through this mechanism, NMD prevents the production of potentially toxic truncated proteins [1]. In addition to its role as a quality control mechanism, NMD also serves to regulate the expression of physiological transcripts that mimic NMD substrates. Such transcripts include a cassette exon containing a PTC, upstream open reading frames, or long 3' untranslated regions. Additionally, intricate auto- and cross-regulatory feedback loops have evolved that utilize NMD to titrate the level of various splicing factors. An excess amount of these splicing factors facilitates the inclusion of a PTC-containing exon which reduces gene expression ("unproductive splicing") [2, 3]. Due to its dual role as a quality control and gene regulatory mechanism, NMD efficiency is modulated in a variety of physiological contexts including cell stress, differentiation, and development [4-7]. NMD is also therapeutically targeted to allow the production of certain truncated proteins that retain residual function to counter loss-of-function genetic diseases [8]. In both scenarios, it remains an open question whether NMD inhibition has broader deleterious consequences for the cell.

Depletion of proteins involved in NMD, as well as pharmacological inhibition of NMD, has been shown to upregulate thousands of aberrant transcripts that are typically degraded by NMD [1, 9-11]. However, whether such transcripts produce truncated proteins is not known. At an organismal level, NMD inhibition has been shown to be immunogenic [12, 13], hinting at the production of truncated proteins with neoantigenic epitopes, although the identity of such proteins has not been characterized.

In this study, we took advantage of a cellular model of a human genetic disease, facioscapulohumeral muscular dystrophy (FSHD), where NMD is naturally inhibited and therefore we could investigate the molecular and functional consequences of the loss of NMD. FSHD is a prevalent progressive myopathy caused by misexpression of a double homeodomain transcription factor, DUX4, in skeletal muscle [14, 15]. DUX4 is normally expressed during early embryonic development where it activates the first wave of zygotic gene expression [16-18]. However, in individuals with FSHD, DUX4 is reactivated in the muscle and induces apoptotic death leading to skeletal muscle atrophy [19-22]. We have shown that DUX4 misexpression in

78   muscle cells causes rapid and acute inhibition of NMD followed by proteotoxic stress and,

79   eventually, translation inhibition [23, 24].

80

81   Here, we asked whether aberrant RNAs stabilized by DUX4-mediated NMD inhibition produce

82   truncated proteins by performing paired RNA-sequencing (RNA-seq) and ribosome profiling

83   (Ribo-seq) at 0, 4, 8, and 14 hours (h) following the expression of DUX4 in MB135-iDUX4

84   human skeletal muscle myoblasts, a well-characterized cellular model of FSHD [25, 26]. While

85   RNA-seq measures transcript abundance, Ribo-seq measures ribosome density along an

86   mRNA [27]. Thus, Ribo-seq serves as a proxy for active translation and allows precise

87   delineation of translation start and end sites in order to characterize the protein products made

88   from aberrant RNAs. Using Ribo-seq, we found that hundreds of aberrant RNAs, stabilized by

89   DUX4-mediated inhibition of NMD, are actively translated to produce truncated proteins –

90   particularly truncated RNA-binding proteins (RBPs) and splicing factors. We show that one such

91   truncated splicing factor, serine/arginine-rich splicing factor 3 (SRSF3-TR), is expressed in

92   FSHD muscle cell cultures and contributes to DUX4 toxicity. Thus, our findings demonstrate that

93   NMD inhibition results in the widespread production of truncated proteins with deleterious

94   cellular consequences.

95   **RESULTS**

96

97   **DUX4 expression allows functional exploration of the consequences of acute NMD**

98   **inhibition.** Misexpression of DUX4 in skeletal muscle cells inhibits NMD and induces

99   cytotoxicity [22, 26, 28]. To identify time points at which to measure transcript- and translation-

100   level changes induced by DUX4 before the onset of overt cytotoxicity, we utilized a well-

101   characterized doxycycline-inducible DUX4 human myoblast line, MB135-iDUX4 [26], harboring

102   a DUX4-responsive mCherry fluorescent reporter (**Figure 1A**). We live imaged these cells every

103   15 min for 28 h following doxycycline treatment to induce DUX4 (**Figure 1A**, **Video 1**).

104   Expression of the DUX4-responsive mCherry was rapid and nearly synchronous, with

105   fluorescence detection after 2 h. Cytotoxicity was first observed 9 h following DUX4 induction,

106   with most cells dead or dying by 18 h (**Video 1**). Western blot analysis showed that levels of the

107   key NMD factor UPF1 were reduced to 47% after only 2 h of DUX4 induction and continued to

108   decrease (**Figure 1B**). This confirmed our previous observation that NMD inhibition is an early

109   event during DUX4 expression [23]. Given these data, we chose the time points of 4, 8, and 14

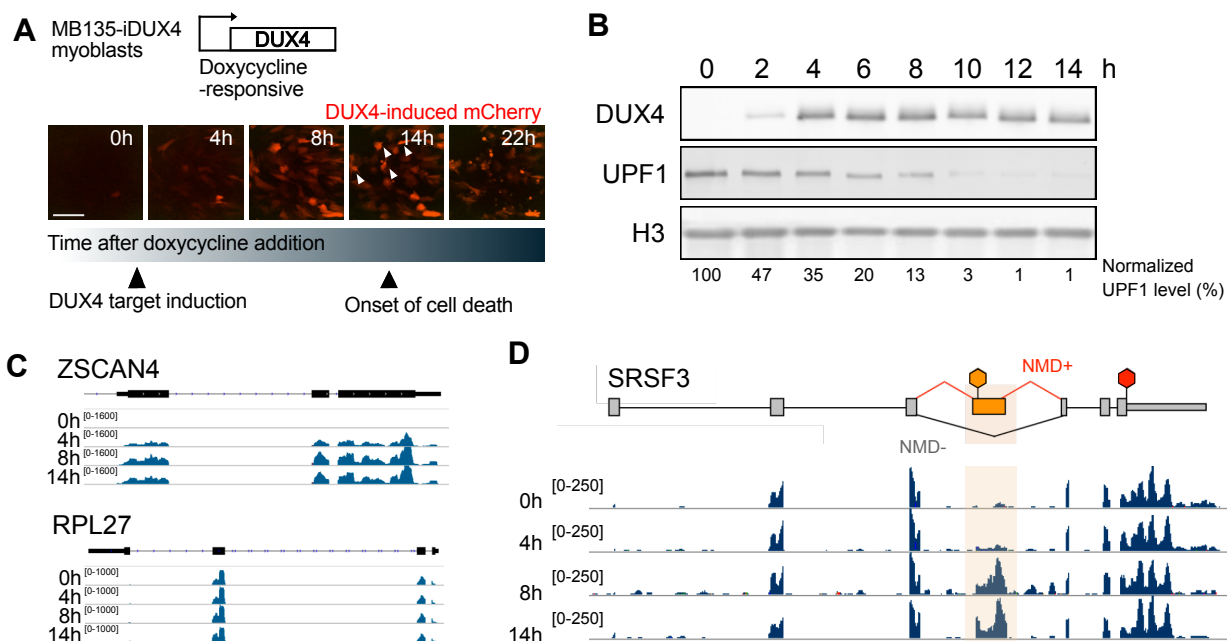110   h post-DUX4 induction to investigate the consequences of NMD inhibition by DUX4.

Figure 1. Synchronous expression of DUX4 in MB135-iDUX4 myoblasts enables time course analyses of downstream gene expression changes. (**A**) Representative images from live cell fluorescence microscopy of MB135-iDUX4/ZSCAN4-mCherry myoblasts following treatment with doxycycline to induce DUX4. Arrowheads indicate overtly dying cells. Scale bar, 150 μm. (**B**) Western blot analysis for DUX4, UPF1, and Histone H3 (loading control) over a time course of DUX4 expression following doxycycline induction in MB135-iDUX4 myoblasts. (**C**) RNA-seq read coverage over a time course of DUX4 expression for DUX4 target gene ZSCAN4 (top) and housekeeping gene RPL27 (bottom). (**D**) RNA-seq coverage over SRSF3. The PTC-containing exon 4 is highlighted. The red hexagon indicates the normal stop codon while the orange hexagon denotes the PTC.

111   First, we examined DUX4-induced transcriptome changes revealed by our RNA-seq dataset

112   (**Supplementary Table 1**). As expected, transcripts of a DUX4 target gene, *ZSCAN4*, were

113   absent in uninduced cells but highly expressed at 4 h and increased with time **(Figure 1C**, top),

114   while the housekeeping gene *RPL27* had constant, robust RNA expression throughout the time

115   course **(Figure 1C**, bottom). Also as expected, aberrant transcript isoforms with PTC-containing

116   exons, such as *SRSF3*, were present at very low levels prior to DUX4 expression but increased

117   in abundance thereafter, appearing as early as 4 h post-induction (**Figure 1D**).

118

119   Genome-wide, DUX4 altered the expression of thousands of transcripts, with known DUX4

120   targets [25] showing increasing upregulation throughout the time course (**Figure S1A**). Using K-

121   means clustering, we grouped the genes significantly altered (defined as absolute log2 fold

122   change > 1 and adjusted p-value < 0.01) at any point during the time course into five clusters

123   (**Figure S1B**) and carried out gene ontology (GO) analysis on each cluster (**Figure S1C**,

124   **Supplementary Table 2**). The genes rapidly induced upon DUX4 expression (Cluster 1) are

125   enriched for negative regulation of cell differentiation, positive regulation of cell proliferation, and

126   DNA-templated transcription, while those rapidly silenced upon DUX4 expression (Cluster 5) are

127   enriched for myogenesis, positive regulation of cell differentiation, and cytoskeleton

128   organization. Together, this is illustrative of a general switch away from a differentiated muscle

129   program and towards a proliferative phenotype, which is consistent with DUX4's normal role in

130   establishing an early embryonic program. Interestingly, the cluster of genes induced only at the

131   late 14 h time point (Cluster 3) is enriched for GO categories mRNA splicing, ribonucleoprotein

132   transport, ubiquitin-dependent process, unfolded protein response, and hypoxia, which have all

133   been previously reported as major signatures of DUX4-induced gene expression [22, 26, 28].

134   Together, these RNA-seq data show that the 4, 8, and 14 h time points capture the temporal

135   range of DUX4-induced gene expression changes, and are consistent with early induction of

136   transcriptional responses and late induction of cell stress response.

137

138   **Ribosome profiling shows concordance between transcript levels and ribosome**

139   **occupancy upon DUX4 expression.** Previous quantitative analysis of the DUX4-induced

140   proteome via stable isotope labeling by amino acids in cell culture (SILAC) mass spectrometry

141   showed discordant changes at the RNA versus protein level [24] raising the possibility that

142   translation could be modulated upon DUX4 expression. Additionally, at later time points DUX4

143   induces dsRNA-mediated activation of PKR [29] and stimulates PERK via the unfolded protein

6

144   response pathway [24], resulting in eIF2α phosphorylation, which is known to inhibit cap-

145   dependent translation [30]. Therefore, we asked whether transcript level changes driven by

146   DUX4 expression were echoed at the level of translation by comparing the RNA-seq and Ribo-

147   seq datasets.

148

149   The characteristic 3 nucleotide periodicity exhibited by the ribosome-protected RNA fragments

150   confirmed the high quality of our Ribo-seq data (**Figure S2**). Representative Ribo-seq read

151   coverage plots of the DUX4 target gene, *ZSCAN4*, showed no coverage in uninduced cells, low

152   ribosome density beginning at 4 h, and active translation at 8 and 14 h (**Figure 2A**, top). In

153   contrast, housekeeping gene *RPL27* showed constant, robust translation throughout the time

154   course (**Figure 2A**, bottom). The changes in ribosome-association at these specific genes

155   mirrored the differences seen in their mRNA levels (**Figure 1C**).

156

157   On a genome scale, DUX4 altered the translation status for thousands of transcripts, with later

158   time points showing larger differences and known DUX4 targets being translated at increasing

159   levels throughout the time course (**Figure 2B**, **Supplementary Table 3**). Most genes were

160   concordantly up or downregulated at the level of transcript and inferred translation efficiency

161   (**Figure 2C**, Materials and Methods) at all time points with only a small number of genes

162   showing some discordance. GO analysis of the discordantly regulated genes returned

163   significant results only for the gene set that showed a mild translation downregulation at the 14

164   h time point (n = 137) with pathways such as protein targeting to ER and viral transcription

165   being enriched which, strikingly, were driven entirely by a group of ribosomal protein-encoding

166   genes (**Supplementary Table 3**). This mild downregulation of translation is consistent with

167   induction of the integrated stress response (ISR) pathway and DUX4-mediated eIF2α

168   phosphorylation [24, 29]. A caveat of Ribo-seq to keep in mind here is that it may not capture

169   the true absolute change in translation efficiency induced by ISR, and therefore the translation

170   downregulation we observe could be an underestimate.

171

172   Nonetheless, we observe several hallmarks of ISR activation at 14 h, including robust

173   translation upregulation of ATF4 (**Figure 2C-D**). Specifically, the start-stop regulatory element in

174   the 5' untranslated region of ATF4, which modifies downstream re-initiation to enhance ATF4's

175   inducibility under stress [31], is highly occupied by ribosomes at 14 h (**Figure 2D**). The resultant

176   upregulation of ATF4 protein can account for the subsequent transcriptional and translational

177   induction of the ATF4 targets GADD34 and ATF3 (**Figure 2E-F**). These data confirm the DUX4-

178   induced phosphorylation of eIF2α via PKR and PERK activation culminate in a block in cap-

179   dependent translation, and stimulation of robust ISR signaling at the late 14 h time point (**Figure**

180   **2G**). Yet, in large part DUX4-induced changes in transcript level are mirrored in their ribosome
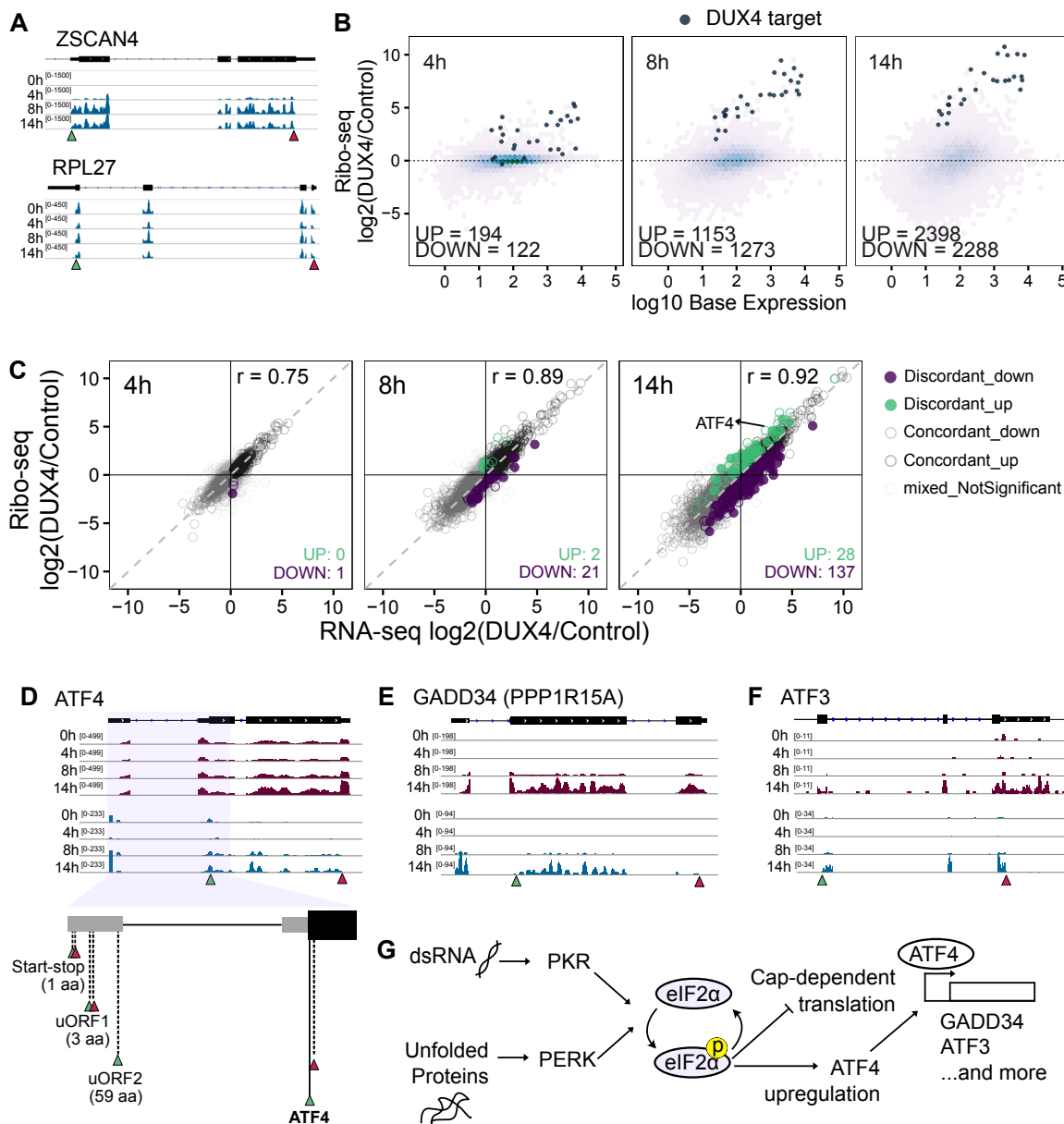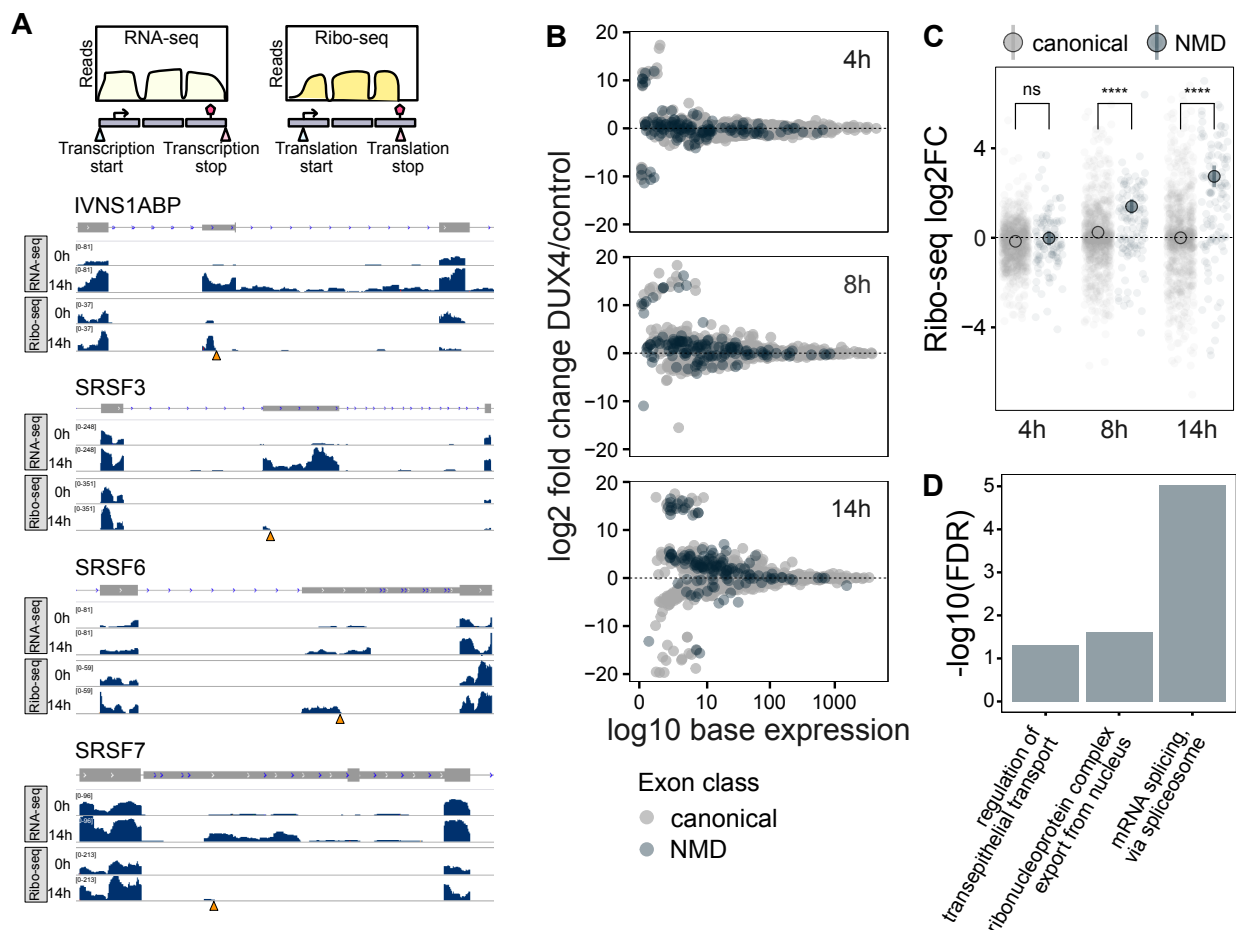
181   occupancy.

Figure 2. Ribo-seq shows high concordance between transcript levels and translation status. (**A**) Ribo-seq read coverage over a time course of DUX4 expression for DUX4 target gene ZSCAN4 (top) and housekeeping gene RPL27 (bottom). Green triangle, translation start. Red triangle, translation stop. (**B**) M-A plots for Ribo-seq data after 4, 8, and 14 h of DUX4 induction compared to the 0 h control. (**C**) Scatter plot of RNA-seq versus Ribo-seq log2 fold change after 4, 8, and 14 h of DUX4 expression. Significance defined as adjusted p-value < 0.01 for Ribo-seq fold change. (**D**) RNA-seq (top) and Ribo-seq (middle) coverage over ATF4; schematic showing the upstream (uORF) and main open reading frames of ATF4 (bottom). (**E-F**) RNA-seq (top) and Ribo-seq (bottom) coverage over GADD34 (**E**) and ATF3 (**F**). (**G**) A schematic summary of how DUX4 expression influences translation and subsequent cell stress.

182

183 **DUX4 causes widespread truncated protein production.** Having shown that most transcripts

184 induced by DUX4 are robustly translated, and that NMD inhibition is an early consequence of

185 DUX4 expression, we sought to determine whether truncated proteins are produced from PTC-

186 containing RNAs stabilized by DUX4-mediated NMD inhibition. Strikingly, when we compared

187 the RNA-seq and Ribo-seq reads at candidate genes with NMD isoforms, IVNS1ABP, SRSF3,

188 SRSF6, and SRSF7, we saw robust coverage across the PTC-containing exon with reads

189 stopping at the PTC (**Figure 3A**). This clearly indicates the translation of truncated proteins from

190 NMD isoforms.

191

192 To systematically ask if and when aberrant RNAs are translated on a genome-level, we used

193 ORFquant [32], a new pipeline that identifies isoform-specific translation events from Ribo-seq

194 data. We then used DEXSeq [33] to conduct exon-level differential analysis on the set of

195 ORFquant-derived open reading frames, using Ribo-seq data. This analysis identifies changes

196 in relative exon usage to measure differences in the expression of individual exons that are not

197 simply the consequence of changes in overall transcript level. After 4 h of DUX4 induction 397

198 genes showed differential expression of specific exons, of which 24 are predicted NMD targets

199 (**Figure 3B**), whereas later time points showed a greater number of exons (n = 96 at 14 h) that

200 are unique to NMD targets as differentially expressed (**Supplementary Table 4**). We grouped

201 exons based on their NMD target status and calculated their fold change in ribosome footprints

202 at 4, 8, and 14 h of DUX4 expression compared to the 0 h time point (**Figure 3C**). We observed

203 a progressive and significant increase in the translation status of NMD-targeted exons, but not

204 canonical exons, at 8 and 14 h, confirming the translation of stabilized aberrant RNAs in DUX4-

205 expressing cells.

206

207 Translation of an NMD target typically generates a prematurely truncated protein. To ask how

208 the specific truncated proteins being produced in DUX4-expressing myoblasts might functionally

209 impact cell homeostasis, we conducted GO analysis of the 74 truncated proteins being actively

210 translated at 14 h of DUX4 induction (**Figure 3D**, **Supplementary Table 4**). Strikingly, the

211 truncated proteins are enriched for genes encoding RBPs involved in mRNA metabolism and

212 specifically, splicing (**Supplementary Table 4**). Thus, not only are NMD targets stabilized by

213 DUX4 expression, but they also produce truncated versions of many RBPs, which could have

214 substantial downstream consequences to mRNA processing in DUX4-expressing cells.

Figure 3. Exon-level analysis of *de novo* identified ORFs from Ribo-seq data demonstrates robust translation of NMD-targeted aberrant RNAs. (A) Schematic representation of the paired RNA-seq and Ribo-seq experiment (top) and RNA-seq and Ribo-seq coverage over splicing-related genes IVNS1ABP, SRSF3, SRSF6, and SRSF7 (bottom). Orange triangles denote PTCs. (**B**) M-A plot of exon-level analysis of Ribo-seq data from 4, 8, and 14 h of DUX4 induction. The x-axis represents mean expression calculated at the level of each exon within a gene. (**C**) Exon-level log2 fold change Ribo-seq values at 4, 8, or 14 h of DUX4 expression for canonical and NMD exons. Statistical testing was performed using a two-sided Wilcoxon test. (**D**) GO analysis results of selected gene sets (biological process complete) for all NMD targets that are translated at 14 h.

215

216   **Truncated SRSF3 is present in FSHD myotubes and contributes to cytotoxicity.** To

217   explore the role of truncated proteins in DUX4-induced cellular phenotypes, we chose SRSF3

218   for further characterization. SRSF3 is an SR family protein that possesses an N-terminal RNA-

219   binding RNA recognition motif (RRM) and a C-terminal arginine/serine (RS)-rich domain

220   responsible for protein-protein and protein-RNA interactions. The NMD isoform of SRSF3

221   encodes a truncated protein (SRSF3-TR) that lacks most of the RS domain and has been

222   previously implicated in a variety of human pathologies [34-38]. Examination of our Ribo-seq

223   data revealed robust expression and translation of SRSF3 NMD-targeted exon 4 that ends at

224   the site of the PTC (**Figure 4A**).

10

225

226   To determine the translation status of the aberrant SRSF3 transcript stabilized by DUX4, we

227   carried out polysome profiling using sucrose density gradient separation. The polysome profile

228   after 14 h of DUX4 expression compared to control showed a higher fraction of 80S compared

229   to polysomes (**Figure 4B**, top left). This is consistent with our prior observation of eIF2α

230   phosphorylation [24, 29] and resultant global downregulation of translation at 14 h. We extracted

231   RNA from various fractions and profiled RNA levels of specific transcripts by qPCR. *RPL27*

232   mRNA was predominantly ribosome-bound in control cells but this partially shifted to

233   monosomes in DUX4-expressing cells (**Figure 4B**, top right). The loss of transcripts from

234   polysome fractions was even more stark for the normal SRSF3 isoform (SRSF3 NMD-) which

235   decreased substantially in DUX4-expressing myoblasts compared to control (**Figure 4B**, bottom

236   left). In striking contrast to both RPL27 and SRSF3 NMD-, the NMD-targeted isoform of SRSF3

237   (SRSF3 NMD+) showed a massive increase in heavy polysomes in DUX4-expressing cells

238   (**Figure 4B**, bottom right). These data show that aberrant SRSF3 mRNA is being actively

239   translated into truncated protein in DUX4-expressing myoblasts and validate the ribosome

240   footprints found on the NMD+ isoform.

241

242   To determine if we could stably detect truncated SRSF3 protein in cells, we generated an

243   antibody recognizing a 10 amino acid C-terminal neo-peptide unique to SRSF3-TR. This custom

244   SRSF3-TR antibody was able to recognize FLAG-tagged SRSF3-TR exogenously expressed in

245   293T cells and endogenous SRSF3-TR immunoprecipitated from DUX4-expressing MB135-

246   iDUX4 myoblasts (**Figure 4C**). We also used a commercial SRSF3 antibody that recognizes an

247   N-terminal epitope common to both the full-length and truncated SRSF3. This antibody detected

248   both exogenously expressed full-length and truncated FLAG-SRSF3, and endogenous full-

249   length SRSF3, but was insufficient to visualize endogenous SRSF3-TR (**Figure 4C**), possibly

250   due to lower affinity for this protein isoform in an immunoprecipitation assay. To determine if

251   SRSF3-TR was present in FSHD myotubes expressing endogenous levels of DUX4, we carried

252   out immunofluorescence for SRSF3-TR or DUX4 in differentiated FSHD and control muscle

253   cells. While there was no detectable SRSF3-TR staining in control cells, in DUX4-expressing

254   FSHD cultures SRSF3-TR appeared in cytoplasmic puncta (**Figure 4D**). Thus, not only is

255   SRSF3 NMD+ isoform translated robustly in DUX4-expressing cells, its protein product, SRSF3-

256   TR can be detected in both DUX4-expressing MB135-iDUX4 myoblasts and in FSHD patient-
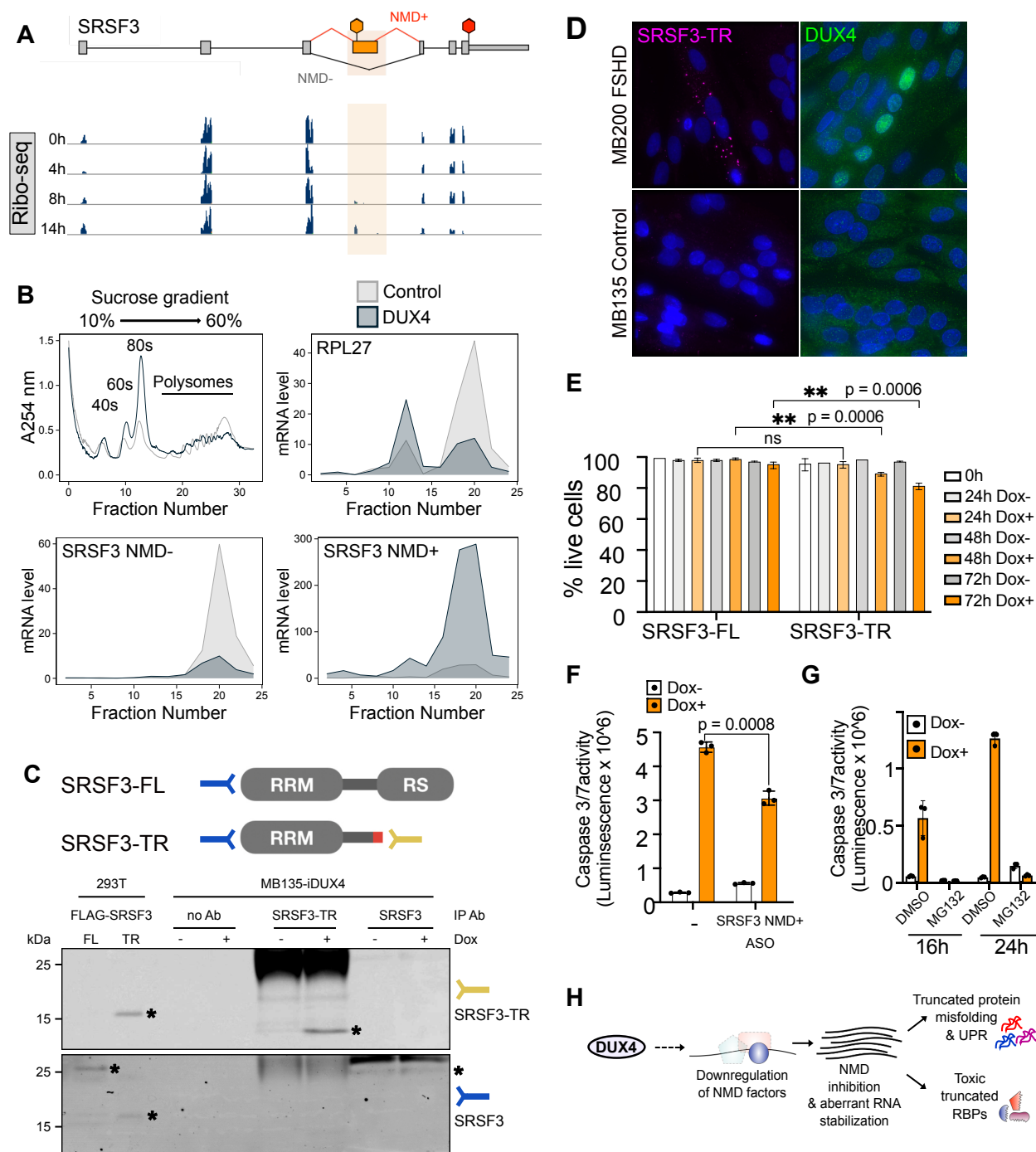
257   derived myotubes.

Figure 4. Truncated SRSF3 protein could disrupt RNA processing in FSHD myotubes. (**A**) Ribo-seq coverage over SRSF3. The PTC-containing exon 4 is highlighted. The red hexagon indicates the normal stop codon while the orange hexagon denotes the PTC. (**B**) Absorbance at 254 nm across a sucrose density gradient of lysates from control MB135-iDUX4 myoblasts and MB135-iDUX4 myoblasts expressing DUX4 for 14 h (top left). RT-qPCR measurement of RPL27, SRSF3 NMD-, and SRSF3 NMD+ mRNA levels in DUX4-expressing myoblasts relative to control myoblasts from collected fractions (remaining panels). (**C**) Detection of SRSF3 and SRSF3-TR in whole cell extracts from 293T cells exogenously expressing FLAG-tagged full-length (FL) or truncated (TR) SRSF3 as compared to protein lysates from MB135-iDUX4 myoblasts treated with (+) or without (-) doxycycline (Dox) to induce DUX4 and immunoprecipitated with a custom anti-SRSF3-TR antibody, no antibody (Ab), or a commercial SRSF3 antibody. IP, immunoprecipitation. Asterisks denote proteins of interest. (**D**) Immunofluorescence staining in MB135 control and MB200 FSHD myotubes differentiated for 72 h and stained with DAPI (blue) and rabbit anti-DUX4 (green)

12

or custom rabbit anti-SRSF3-TR (pink) antibody. (**E**) Trypan blue exclusion-based live cell counts in myoblasts expressing doxycycline (Dox)-inducible full-length (FL) or truncated (TR) SRSF3. Error bars denote the standard deviation from the mean of three biological replicates. (**F**) Caspase 3/7 activity following ASO-mediated knockdown of SRSF3 NMD+ in MB135-iDUX4 myoblasts left untreated (Dox-) or treated with doxycycline for 16 h (Dox+) to induce DUX4. Error bars denote the standard deviation from the mean of three biological replicates. (**G**) Cell viability as measured by Caspase 3/7 activity following co-treatment with doxycycline (Dox) to induce DUX4 and proteasome inhibition via MG132 treatment for 16 or 24 h. (**H**) Schematic representation of a working model where DUX4-induced downregulation of NMD factors stabilizes aberrant RNAs producing truncated RBPs and misfolded proteins that trigger the unfolded protein response and toxicity.

258

259   To ask if expression of SRSF3-TR is deleterious to cells, we exogenously expressed FLAG-

260   tagged full-length or truncated SRSF3 in healthy muscle cells via lentiviral transduction. We

261   found that SRSF3-TR, but not SRSF3-FL, reduced the viability of MB135 myoblasts (**Figure**

262   **4E**). To specifically knock down the SRSF3-TR isoform in DUX4-expressing myoblasts, we

263   screened several antisense oligonucleotides (ASOs) in order to identify one (a thiomorpholino

264   2'-deoxyribonucleotide 3'-thiophosphate oligonucleotide chimera [39, 40]) that lowered the

265   SRSF3-TR isoform without significantly impacting DUX4 transcript level or target expression

266   (**Figure S3**). Treatment of DUX4-expressing myoblasts with this thiomorpholino oligonucleotide

267   resulted in a 34% reduction in cell death compared to untreated cells (**Figure 4F**). Finally, we

268   found that blocking the proteasome, which is the primary mediator of NMD inhibition by DUX4,

269   robustly rescues DUX4 toxicity (**Figure 4G**). These results suggest that truncated proteins

270   confer toxicity to muscle cells via a gain-of-function mechanism. Significantly, this mechanism is

271   potentially additive across the different species of truncated proteins that are robustly made

272   upon DUX4 expression in myoblasts (**Figure 4H**).

273   **DISCUSSION**

274   Loss of NMD leads to the stabilization of aberrant RNAs [41]. However, it is not known whether

275   these aberrant RNAs are translated and what proteins they might produce. Here, we paired

276   RNA-seq and Ribo-seq across a time course of DUX4 expression in human skeletal muscle

277   myoblasts to demonstrate that DUX4-induced NMD inhibition indeed causes truncated protein

278   production at a genome level.

279

280   The production of truncated proteins upon NMD inhibition by DUX4 has multiple implications at

281   both molecular and functional levels. Protein truncation could result in a dominant negative

282   function that inhibits the activity of the remaining, cell critical full-length protein. Truncated

283   proteins might misfold and facilitate the formation of protein aggregates. And finally, some

284   truncated proteins contain unique C-terminal extensions, or neo-peptides, that could serve as

285   novel antigens and might induce inflammation. Hence, when NMD is modulated as a

286   therapeutic intervention for genetic diseases, it is important to consider whether truncated

287   proteins are produced as a consequence, and whether this might have a negative impact. In

288   physiological contexts where NMD efficiency is suppressed without negative consequences,

289   cells may possess mechanisms that counter truncated protein production. Further investigation

290   of the suppression or tolerance of truncated proteins in these contexts would reveal new

291   mechanisms that enable the protein quality control rheostat to be adjusted to deal with variable

292   NMD efficiencies.

293

294   In FSHD, there is evidence for truncated proteins contributing to myotoxicity via all of the above

295   mechanisms. Here, we show gain-of-function toxicity for SRSF3-TR. Prior work has

296   demonstrated protein aggregation [29, 42, 43], as well as immune cell infiltration [44-47] in

297   FSHD muscle. Our results suggest that these effects could be due to truncated proteins and

298   neoantigenic epitopes. In addition, many of the identified DUX4-induced truncated proteins are

299   RBPs and splicing factors. It is well-established that DUX4 alters RNA splicing [22, 24, 26, 28]

300   and therefore interesting to speculate that truncated RBPs and splicing proteins might be

301   responsible for inducing global RNA processing defects [48]. Such misprocessing would

302   generate aberrant RNAs that could act to further overwhelm the already inhibited NMD pathway.

303

304   In summary, we demonstrate the widely-held but previously unproven assumption that NMD

305   inhibition indeed results in the production of truncated proteins with deleterious cellular

306   consequences. In doing so, we provide a framework to interpret the multifaceted phenotypes

307   observed in FSHD as a potential result of NMD inhibition. Our findings provide a critical missing

308   piece in the understanding of this essential quality control mechanism in both disease and

309   physiology, which has implications for treatment of genetic diseases.

310 **MATERIALS AND METHODS**

311

312 **RESOURCE AVAILABILITY**

313

314 **Lead contact**

315 Further information and requests for resources and reagents should be directed to and will be

316 fulfilled by the lead contact, Sujatha Jagannathan (sujatha.jagannathan@cuanschutz.edu).

317

318 **Materials availability**

319 The cell lines and antibody generated in this study are available upon request. Plasmids

320 generated in this study have been deposited to Addgene (plasmid #171951, #171952, #172345,

321 and #172346).

322

323 **Data and code availability**

324 The RNA-seq and Ribo-seq data generated during this study are available at GEO (accession

325 number GSE178761). The code generated during this study are available at GitHub

326 (https://github.com/sjaganna/2021-campbell_dyle_calviello_et_al).

327

328 **EXPERIMENTAL MODEL AND SUBJECT DETAILS**

329

330 **Cell lines and culture conditions**

331 293T cells were obtained from ATCC (CRL-3216). MB135, MB135-iDUX4, MB135-

332 iDUX4/ZSCAN4-mCherry, and MB200 immortalized human myoblasts were a gift from Dr.

333 Stephen Tapscott and originated from the Fields Center for FSHD and Neuromuscular

334 Research at the University of Rochester Medical Center. MB135-iDUX4 cells have been

335 described previously [26]. MB135-iFLAG-SRSF3-FL, and MB135-iFLAG-SRSF3-TR

336 immortalized human myoblasts were generated in this study. All parental cell lines were

337 authenticated by karyotype analysis and determined to be free of mycoplasma by PCR

338 screening. 293T cells were maintained in Dulbecco's Modified Eagle Medium (DMEM) (Thermo

339 Fisher Scientific) supplemented with 10% EqualFETAL (Atlas Biologicals). Myoblasts were

340 maintained in Ham's F-10 Nutrient Mix (Thermo Fisher Scientific) supplemented with 20% Fetal

341 Bovine Serum (Thermo Fisher Scientific), 10 ng/mL recombinant human basic fibroblast growth

342 factor (Promega), and 1 μM dexamethasone (Sigma-Aldrich). MB135-iDUX4/ZSCAN4-mCherry

343 and MB135-iDUX4 myoblasts were additionally maintained in 2 μg/mL puromycin

16

344   dihydrochloride (VWR). MB135-iFLAG-SRSF3-FL and -TR myoblasts were additionally

345   maintained in 10 µg/mL blasticidin S HCl (Thermo Fisher Scientific). Induction of DUX4 and

346   SRSF3 transgenes was achieved by culturing cells in 1-2 µg/mL doxycycline hyclate (Sigma-

347   Aldrich). Differentiation of myoblasts into myotubes was achieved by switching the fully

348   confluent myoblast monolayer into DMEM containing 1% horse serum (Thermo Fisher

349   Scientific) and Insulin-Transferrin-Selenium (Thermo Fisher Scientific). All cells were incubated

350   at 37 °C with 5% CO_2.

351

352   **METHOD DETAILS**

353

354   **Cloning**

355   pTwist-FLAG-SRSF3_Full.Length_Codon.Optimized and pTwist-FLAG-

356   SRSF3_Truncated_Codon.Optimized plasmids were synthesized by Twist Bioscience. To

357   construct pCW57.1-FLAG-SRSF3_Full.Length_Codon.Optimized-Blast and pCW57.1-FLAG-

358   SRSF3_Truncated_Codon.Optimized-Blast plasmids, the SRSF3 open reading frames were

359   subcloned into pCW57-MCS1-P2A-MCS2 (Blast) (a gift from Adam Karpf, Addgene plasmid

360   #80921) [49] by restriction enzyme digest using EcoRI and BamHI (New England Biolabs).

361

362   **Antibody generation**

363   Purified SRSF3-TR peptide (Cys-PRRRVTIMSLLTTL) was used as an immunogen and

364   polyclonal rabbit anti-SRSF3-TR antibody production was done in collaboration with Pacific

365   Immunology (Ramona, CA). The antisera from all animals were screened for reactivity by ELISA

366   against the immunogen and with western blots and immunofluorescence against transfected

367   SRSF3-TR.

368

369   **Transgenic cell line generation**

370   Lentiviral particles expressing doxycycline-inducible FLAG-SRSF3-FL or -TR transgenes were

371   generated by co-transfecting 293T cells with the appropriate lentivector, pMD2.G (a gift from

372   Didier Trono, Addgene plasmid #12259), and psPAX2 (a gift from Didier Trono, Addgene

373   plasmid #12260) using Lipofectamine 2000 Transfection Reagent (Thermo Fisher Scientific). To

374   generate polyclonal SRSF3 transgenic cell lines, MB135 myoblasts were transduced with

375   lentivirus in the presence of 8 µg/mL polybrene (Sigma-Aldrich) and selected using 10 µg/mL

376   blasticidin S HCl.

377

378 **Plasmid transfections**

379 293T cells were transfected with pTwist-FLAG-SRSF3_Full.Length_Codon.Optimized and

380 pTwist-FLAG-SRSF3_Truncated_Codon.Optimized plasmids using Lipofectamine 2000

381 Transfection Reagent following the manufacturer's instructions.

382

383 **Live cell imaging**

384 MB135-iDUX4/ZSCAN4-mCherry myoblasts were induced with doxycycline hyclate to turn on

385 DUX4 expression and subjected to time lapse imaging using the IncuCyte S3 incubator

386 microscope system (Sartorius). Images were collected every 15 min from the time of

387 doxycycline addition (t = 0 h) to 28 h.

388

389 **RNA extraction and RT-qPCR**

390 Total RNA was extracted from whole cells using TRIzol Reagent (Thermo Fisher Scientific)

391 following the manufacturer's instructions. Isolated RNA was treated with DNase I (Thermo

392 Fisher Scientific) and reverse transcribed to cDNA using SuperScript III reverse transcriptase

393 (Thermo Fisher Scientific) and random hexamers (Thermo Fisher Scientific) according to the

394 manufacturer's protocol. Quantitative PCR was carried out on a CFX384 Touch Real-Time PCR

395 Detection System (Bio-Rad) using primers specific to each gene of interest and iTaq Universal

396 SYBR Green Supermix (Bio-Rad). The expression levels of target genes were normalized to

397 that of the reference gene *RPL27* using the delta-delta-Ct method [50]. The primers used in this

398 study are listed in the Key Resources Table.

399

400 **RNA-seq library preparation and sequencing**

401 Total RNA was extracted from whole cells using TRIzol Reagent following the manufacturer's

402 instructions. Isolated RNA was subjected to ribosomal RNA depletion using the Ribo-Zero rRNA

403 Removal Kit (Illumina). RNA-seq libraries were prepared using the NEXTflex Rapid Directional

404 qRNA-Seq Kit (Bioo Scientific) following the manufacturer's instructions and sequenced using

405 75 bp single-end sequencing on the Illumina NextSeq 500 platform by the BioFrontiers Institute

406 Next-Gen Sequencing Core Facility.

407

408 **Ribosome footprinting**

409 Ribo-seq was performed as described previously [32] using six 70% confluent 10 cm dishes of

410 MB135-iDUX4 cells per condition. Briefly, cells were washed with ice-cold phosphate-buffered

411 saline (PBS) supplemented with 100 µg/mL cycloheximide (Sigma-Aldrich), flash frozen on

18

412   liquid nitrogen, and lysed in Lysis Buffer (PBS containing 1% (v/v) Triton X-100 and 25 U/mL

413   TurboDNase (Ambion)). Cells were harvested by scraping and further lysed by trituration ten

414   times through a 26-gauge needle. The lysate was clarified by centrifugation at 20,000 g for 10

415   min at 4 °C. The supernatants were flash frozen in liquid nitrogen and stored at -80 °C. Thawed

416   lysates were treated with RNase I (Ambion) at 2.5 U/µL for 45 min at room temperature with

417   gentle mixing. Further RNase activity was stopped by addition of SUPERaseIn RNase Inhibitor

418   (Thermo Fisher Scientific). Next, ribosome complexes were enriched using MicroSpin S-400 HR

419   Columns (GE Healthcare) and RNA extracted using the Direct-zol RNA Miniprep Kit (Zymo

420   Research). Ribo-Zero rRNA Removal Kit was used to deplete rRNAs and the ribosome-

421   protected fragments were recovered by running them in a 17% Urea gel, staining with SYBR

422   Gold (Invitrogen), and extracting nucleic acids that are 27 to 30 nucleotides long from gel slices

423   by constant agitation in 0.3 M NaCl at 4 °C overnight. The recovered nucleic acids were

424   precipitated with isopropanol using GlycoBlue Coprecipitant (Ambion) as carrier and treated with

425   T4 polynucleotide kinase (Thermo Fisher Scientific). Libraries were prepared using the

426   NEXTflex Small RNA-Seq Kit v3 (Bioo Scientific) following the manufacturer's instructions and

427   sequenced using 75 bp single-end reads on an Illumina NextSeq 500 by the BioFrontiers

428   Institute Next-Gen Sequencing Core Facility.

429

430   **RNA-seq and Ribo-seq data analysis**

431   Fastq files were stripped of the adapter sequences using cutadapt. UMI sequences were

432   removed, and reads were collapsed to fasta format. Reads were first aligned against rRNA

433   (accession number U13369.1), and to a collection of snoRNAs, tRNAs, and miRNA (retrieved

434   using the UCSC table browser) using bowtie2 [51]. Remaining reads were mapped to the hg38

435   version of the genome (without scaffolds) using STAR 2.6.0a [52] supplied with the GENCODE

436   25 .gtf file. A maximum of two mismatches and mapping to a minimum of 50 positions was

437   allowed. De-novo splice junction discovery was disabled for all datasets. Only the best

438   alignment per each read was retained. Quality control and read counting of the Ribo-seq data

439   was performed with Ribo-seQC [53].

440

441   Differential gene expression analysis of the RNA-seq data was conducted using DESeq2 [54].

442   Briefly, featureCounts from the subread R package [55] was used to assign aligned reads (in

443   BAM format) to genomic features supplied with the GENCODE 25. gtf file. The featureCounts

444   output was then supplied to DESeq2 and differential expression analysis was conducted with

445   the 0 h time point serving as the reference sample. Genes with very low read count were filtered

446 out by requiring at least a total of 10 reads across the 12 samples (3 replicates each of the 0, 4,

447 8, and 14 h samples). Log2 fold change shrinkage was done using the apeglm function [56].

448

449 Differential analysis of the RNA-seq and Ribo-seq data was performed using DESeq2, as

450 previously described [57, 58], using an interaction model between the tested condition and

451 RNA-seq – Ribo-seq counts. Only reads mapping uniquely to coding sequence regions were

452 used. In addition, ORFquant [32] was used to derive de-novo isoform-specific translation

453 events, by pooling the Ribo-seQC output from all Ribo-seq samples, using uniquely mapping

454 reads. DEXSeq [33] was used to perform differential exon usage along the DUX4 time course

455 data, using Ribo-seq counts on exonic bins and junctions belonging to different ORFquant-

456 derived translated regions. NMD candidates were defined by ORFquant as open reading frames

457 ending with a stop codon upstream of an exon-exon junction.

458

459 **GO category analysis**

460 Gene Ontology (GO) analysis was conducted using the web tool http://geneontology.org,

461 powered by pantherdb.org. Briefly, statistical overrepresentation test using the complete GO

462 biological process annotation dataset was conducted and p-values were calculated using the

463 Fisher's exact test and False Discovery Rate was calculated by the Benjamini-Hochberg

464 procedure.

465

466 **Polysome profiling**

467 Polysome profiling was performed as previously described [59, 60] with the following

468 modifications. Four 70% confluent 15 cm dishes of MB135-iDUX4 cells per condition were

469 treated with 100 μg/mL cycloheximide for 10 min, transferred to wet ice, washed with ice-cold

470 PBS containing 100 μg/mL cycloheximide, and then lysed in 400 μL Lysis Buffer (20 mM

471 HEPES pH 7.4, 15 mM $MgCl_2$, 200 mM NaCl, 1% Triton X-100, 100 μg/mL cycloheximide, 2

472 mM DTT, and 100 U/mL SUPERaseIn RNase Inhibitor) per 15 cm dish. The cells and buffer

473 were scraped off the dish and centrifuged at 13,000 rpm for 10 min at 4 °C. Lysates were

474 fractionated on a 10% to 60% sucrose gradient using the SW 41 Ti Swinging-Bucket Rotor

475 (Beckman Coulter) at 36,000 rpm for 3 h and 10 min. Twenty-four fractions were collected using

476 a Gradient Station ip (BioComp) and an FC 203B Fraction Collector (Gilson) with continuous

477 monitoring of absorbance at 254 nm. RNA from each fraction was extracted using TRIzol LS

478 Reagent (Thermo Fisher Scientific) following the manufacturer's instructions. RT-qPCR was

479 carried out as described above.

20

480

Protein extraction

Total protein was extracted from whole cells using TRIzol Reagent following the manufacturer's instructions, excepting that protein pellets were dissolved in Protein Resuspension Buffer (0.5 M Tris base, 5% SDS). Isolated protein was quantified using the Pierce BCA Protein Assay Kit (Thermo Fisher Scientific) according to the manufacturer's protocol. Protein was mixed with 4X NuPAGE LDS Sample Buffer (Thermo Fisher Scientific) containing 50 mM DTT and heated to 70 °C before immunoblotting.

Immunoprecipitation

MB135-iDUX4 myoblasts were treated with or without doxycycline for 14 h and then trypsinized prior to lysis on ice in 1 mL of Lysis Buffer (50 mM Tris-HCl pH 7.5, 150 mM NaCl, 1% NP-40) containing protease inhibitors (Sigma Aldrich). Lysates were precleared using Protein G Sepharose (Thermo Fisher Scientific) for 1 h prior to an overnight incubation at 4 °C with either anti-SRSF3 or anti-SRSF3-TR antibody. Protein G Sepharose was added the following morning for 5 h to bind the antibody, and beads were subsequently washed 5 times with 1 mL cold Lysis Buffer. After the final wash, 4X NuPAGE LDS Sample Buffer containing 50 mM DTT was added directly to the beads and samples heated to 70 °C for protein elution before immunoblotting.

Immunoblotting

Protein was run on NuPAGE Bis-Tris precast polyacrylamide gels (Thermo Fisher Scientific) alongside PageRuler Plus Prestained Protein Ladder (Thermo Fisher Scientific) and transferred to Odyssey nitrocellulose membrane (LI-COR Biosciences). Membranes were blocked in Intercept (PBS) Blocking Buffer (LI-COR Biosciences) before overnight incubation at 4 °C with primary antibodies diluted in Blocking Buffer containing 0.2% Tween 20. Membranes were incubated with IRDye-conjugated secondary antibodies (LI-COR Biosciences) for 1 h and fluorescent signal visualized using a Sapphire Biomolecular Imager (Azure Biosystems) and Sapphire Capture software (Azure Biosystems). When appropriate, membranes were stripped with Restore Western Blot Stripping Buffer (Thermo Fisher Scientific) before being re-probed. Band intensities were quantified by densitometry using ImageJ [61].

Immunofluorescence

Cells were fixed in 10% Neutral Buffered Formalin (Research Products International) for 30 min and permeabilized for 10 min in PBS with 0.1% Triton X-100. Samples were then incubated

514   overnight at 4 °C with primary antibodies, followed by incubation with 488- or 594-conjugated

515   secondary antibodies for 1 h prior to counterstaining and mounting with Prolong Diamond

516   Antifade Mountant with DAPI (Thermo Fisher Scientific). Slides were imaged with a DeltaVision

517   Elite deconvolution microscope, CoolSNAP HQ^2 high-resolution CCD camera, and Resolve3D

518   softWoRx-Acquire v7.0 software. Image J software [61] was used for image analysis.

519

520   **Solid phase synthesis of TMO chimeras (ASOs)**

521   TMO chimeras were synthesized according to the previously reported procedure [39, 40].

522   Briefly, the 5'-dimethoxytrityl (DMT) protecting group of the solid supported 2'-

523   deoxyribonucleoside (CPG-500 support, Glen Research) was deprotected in the first stage by

524   using 3% trichloroacetic acid in dichloromethane. In the second stage, condensation of the

525   resulting CPG-500 support linked 5'-hydroxyl-2'-deoxyribonucleoside with the 6'-DMT-

526   morpholinonucleoside 3'-phosphordiamidites of mA^{Bz}, mG^{iBu}, mC^{Bz}, mT (ChemGenes) or

527   commercial 2'-deoxyribonucleoside 3'-phosphoramidites was achieved using 5-ethylthio-1H-

528   tetrazole (ETT) in anhydrous acetonitrile as activator (30 sec condensation time). Subsequent

529   conversion of P(III) linkages to P(V) thiophosphoramidate (TMO) or P(V) 2'-deoxyribonucleoside

530   3'-thiophosphate was achieved by using 3-[(Dimethylaminomethylene)amino]-3H-1,2,4-

531   dithiazole-5-thione (DDTT) as the sulfurization agent. Finally, the unreacted hydroxyl groups

532   were acetylated by conventional capping reagents (Cap A: Tetrahydrofuran/Acetic Anhydride

533   and Cap B: 16% 1-Methylimidazole in Tetrahydrofuran; Glen Research). The 5'-DMT protecting

534   group on the resulting dinucleotide was next deprotected using deblocking mixture and this

535   DMT deprotected dinucleotide was then used for additional cycles in order to generate ASOs

536   having internucleotide thiophosphoramidate or thiophosphate linkages. The above cycle was

537   repeated to provide the thiomorpholino oligonucleotide chimeras of the desired length and

538   sequence. Cleavage of these 5'-protected DMT-on oligonucleotides from the solid support and

539   deprotection of base and phosphorus protecting groups was carried out using 0.5 mL of 28%

540   aqueous ammonia at 55 °C for 16 h. Subsequently, the CPG was filtered through a micro spin

541   centrifuge filter with pore size of 0.2 μm and the resulting filtrate was evaporated to dryness on a

542   SpeedVac (Thermo Fisher Scientific). The residue was dissolved in 0.75 mL of 3%

543   acetonitrile/water mixture and filtered through a micro spin centrifuge filter. A small portion of the

544   crude sample was withdrawn and submitted to LCMS analysis. The remaining reaction mixture

545   was purified by RP-HPLC. Fractions containing the pure ASO were combined, evaporated to

546   dryness, and submitted to LCMS analysis. Fractions containing the pure DMT-on ASO were

547   dissolved in 0.5 mL of detritylation mixture. After 25 min at 40 °C, the mixture was neutralized

548 with 5 µL of triethylamine, filtered using a micro spin centrifuge filter, and the filtrate containing

549 the sample was purified by RP-HPLC column chromatography. Fractions containing the final

550 DMT-off product were combined and evaporated to dryness on a SpeedVac. The residue was

551 submitted to LCMS analysis in order to determine the purity of the sample. The concentration of

552 the ASO was determined by NanoDrop spectrophotometry before storing the samples at -20 °C.

553

554 **LCMS analysis**

555 LCMS analysis was performed on an Agilent 6530 series Q-TOF LC/MS spectrometer. A

556 Waters ACQUITY UPLC® BEH C18, 1.7 µm, 2.1 X 100 nm column was used as the stationary

557 phase. Aqueous phase was Buffer A (950 mL water, 25 mL methanol, 26 mL hexafluoro-2-

558 propanol (HFIP) and 2.5 mL triethyl amine) and organic phase was Buffer B (925 mL methanol,

559 50 mL water, 26 mL hexafluoro-2-propanol (HFIP) and 2.5 mL triethyl amine). The gradient was

560 0-100% of Buffer B for 30 min followed by 100% Buffer B for 5 min at a flow rate of 0.2 mL/min

561 and a set temperature of 25 °C. The observed masses of the ASOs were consistent with the

562 expected theoretical masses.

563

564 **Antisense oligonucleotide transfections**

565 ASOs were transfected into MB135-iDUX4 cells 40 h prior to doxycycline induction using

566 Lipofectamine RNAiMAX Transfection Reagent (Thermo Fisher Scientific) following the

567 manufacturer's instructions. The ASOs used in this study are listed in the Key Resources Table.

568

569 **Cell viability assays**

570 Trypan blue dye was used to determine the viability of MB135-iFLAG-SRSF3-FL and -TR cell

571 lines. Ten microliters of trypsinized and resuspended cells were mixed with 10 µL of 0.4%

572 Trypan Blue Stain (Thermo Fisher Scientific) for 1 min before immediate counting using a

573 hemocytometer and Motic AE2000 inverted light microscope. Caspase 3/7 activity was used to

574 determine the viability of MB135-iDUX4 myoblasts treated with ASOs or proteasome inhibitors.

575 MB135-iDUX4 cells were seeded in 24-well plates at 8e4 cells per well, transfected with ASOs

576 as described above, and 40 h later treated with 2 µg/mL doxycycline hyclate or seeded in 96-

577 well plates at 3e3 cells per well and 24 h later treated with 1 µg/mL doxycycline hyclate and

578 either DMSO or 10 µM MG132 (Sigma-Aldrich). Caspase 3/7 activity was measured 16 and 24

579 h later using the Caspase-Glo 3/7 Assay System (Promega) following the manufacturer's

580 instructions. Luminescence was detected using a GloMax-Multi Detection System (Promega).

581

582 **Antibodies**

583 The antibodies used in this study are anti-DUX4 (Abcam 124699), anti-Histone H3 (Abcam

584 1791), anti-SRSF3 (Thermo Fisher Scientific 33-4200), anti-SRSF3-TR (this paper), anti-

585 RENT1/hUPF1 (Abcam ab109363), Drop-n-Stain CF 488A Donkey Anti-Rabbit IgG (Biotium

586 20950), Drop-n-Stain CF 594 Donkey Anti-Rabbit IgG (Biotium 20951), IRDye 650 Goat anti-

587 Mouse IgG Secondary Antibody (LI-COR Biosciences 926-65010), and IRDye 800CW Goat

588 anti-Rabbit IgG Secondary Antibody (LI-COR Biosciences 926-32211).

589

590 **QUANTIFICATION AND STATISTICAL ANALYSIS**

591

592 **Data analysis, statistical tests, and visualization**

593 All data analysis and statistical tests were performed in the R programming environment and

594 relied on Bioconductor [62] and ggplot2 [63]. Plots were generated using R plotting functions

595 and/or the ggplot2 package. Bar graphs were generated using GraphPad Prism software

596 version 9.0. Biological replicates were defined as experiments performed separately on distinct

597 samples (i.e. cells cultured in different wells) representing identical conditions and/or time

598 points. No outliers were eliminated in this study. Statistical tests were performed using R

599 functions or GraphPad Prism.

ACKNOWLEDGEMENTS

AUTHOR CONTRIBUTIONS

A.E.C., M.C.D., and S.J. conceived and designed the study. A.E.C, M.C.D., M.A.C., and T.F. performed experiments. K.S. and M.H.C. provided the thiomorpholino oligonucleotides. A.E.C., L.C., T.M., R.F., A.E.G., M.H.C., S.N.F., and S.J. analyzed data. A.E.C. and S.J. wrote the paper with input from all authors.

DECLARATION OF INTERESTS

The authors declare no competing interests.
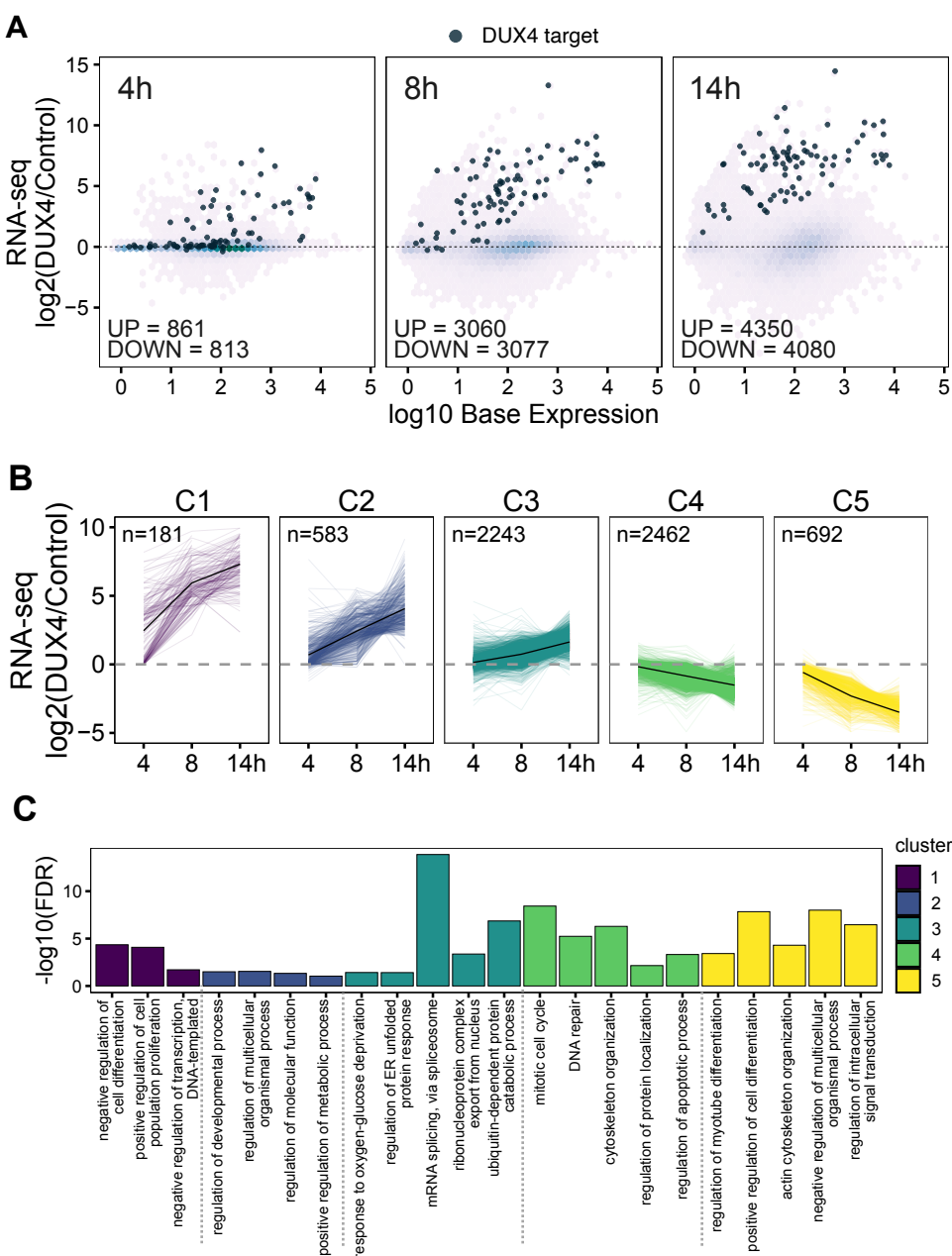
621 **SUPPLEMENTAL FILES**

Figure S1. Time course RNA-seq in MB135-iDUX4 myoblasts reveals early transcript-level changes in pathways underlying FSHD pathology. (**A**) M-A plots for RNA-seq data after 4, 8, and 14 h of DUX4 induction compared to the 0 h control. DUX4 target status defined as in [25]. (**B**) Log2 fold change in RNA expression from the 0 h time point is shown for each gene after k-means clustering. The thick black line represents the cluster mean. (**C**) GO analysis results of selected gene sets (biological process complete) that are significantly enriched in each cluster defined in (**B**).
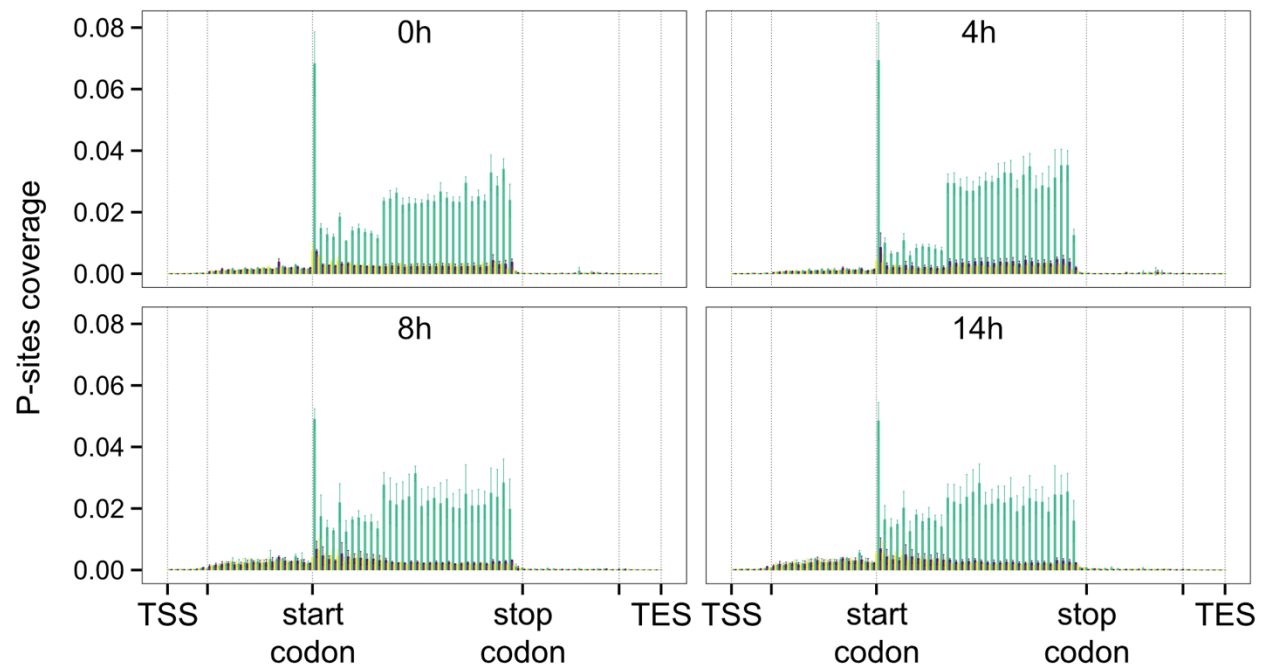
26

Figure S2. Ribo-seq quality control. Aggregate profile of P-sites coverage (as calculated by Ribo-seQC) depicting single nucleotide resolution of Ribo-seq data along the time course. Each frame is shown with a different color. Error bars represent the standard deviation from three biological replicates.
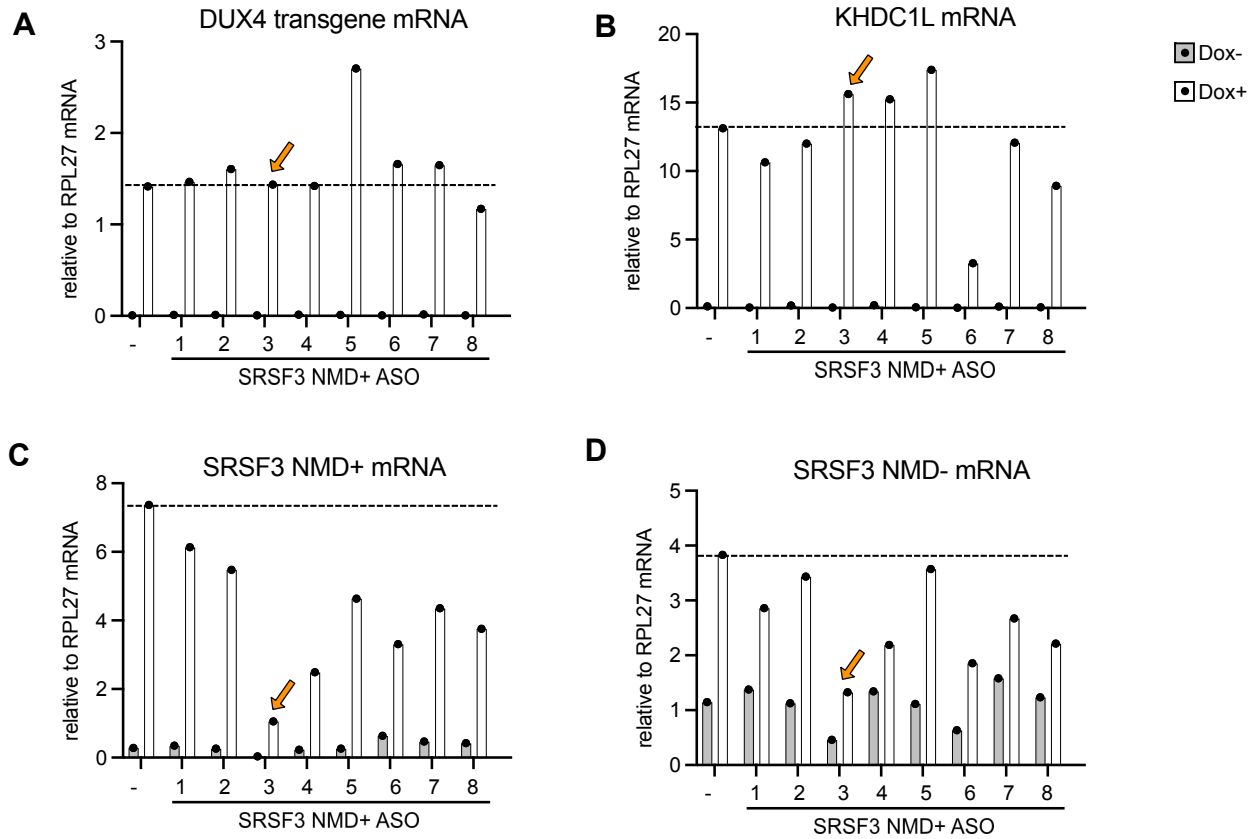
Figure S3. Relative RNA levels of (**A**) DUX4 transgene, (**B**) KHDC1L (DUX4 target gene), (**C**) SRSF3 NMD+, and (**D**) SRSF3 NMD- isoforms as determined by RT-qPCR following transfection with antisense oligos (ASOs) targeting SRSF3 NMD+ and doxycycline (Dox) treatment for 14 h to induce DUX4 in MB135-iDUX4 myoblasts. The tested ASOs are numbered 1-8; "-" indicates no ASO control. The orange arrow indicates the ASO chosen for further studies in Figure 4F.

622 **Video 1. Time course imaging following DUX4 expression.**

623 Live cell fluorescence microscopy recording of MB135-iDUX4/ZSCAN4-mCherry myoblasts

624 treated with doxycycline to induce DUX4 expression.

625

626 **Supplementary Table 1.**

627 DESeq2 differential gene expression analysis results for DUX4 time course RNA-seq data at 4,

628 8, or 14 h post-induction compared to 0 h (control).

629

630 **Supplementary Table 2.**

631 Cluster analysis of RNA-seq log2 fold change at 4, 8, or 14 h of DUX4 induction compared to 0

632 h (control); and Gene Ontology analysis of genes within each cluster.

633

634 **Supplementary Table 3.**

635 ORFquant analysis results for DUX4 time course RNA-seq and Ribo-seq data at 4, 8, or 14 h

636 post-induction compared to 0 h (control); and Gene Ontology analysis of genes with

637 downregulated ribosome density at 14 h.

638

639 **Supplementary Table 4.**

640 DEXSeq analysis results for DUX4 time course Ribo-seq data at 4, 8, or 14 h post-induction

641 compared to 0 h (control); and Gene Ontology analysis of NMD targets upregulated at 14 h.

642   **REFERENCES**

643

644   1.   Mendell JT, Sharifi NA, Meyers JL, Martinez-Murillo F, Dietz HC. Nonsense surveillance

645   regulates expression of diverse classes of mammalian transcripts and mutes genomic noise.

646   Nat Genet. 2004;36(10):1073-8. https://doi.org/10.1038/ng1429

647   2.   Lareau LF, Inada M, Green RE, Wengrod JC, Brenner SE. Unproductive splicing of SR

648   genes associated with highly conserved and ultraconserved DNA elements. Nature.

649   2007;446(7138):926-9. https://doi.org/10.1038/nature05676

650   3.   Ni JZ, Grate L, Donohue JP, Preston C, Nobida N, O'Brien G, et al. Ultraconserved

651   elements are associated with homeostatic control of splicing regulators by alternative splicing

652   and nonsense-mediated decay. Genes Dev. 2007;21(6):708-18.

653   http://www.genesdev.org/cgi/doi/10.1101/gad.1525507

654   4.   Li Z, Vuong JK, Zhang M, Stork C, Zheng S. Inhibition of nonsense-mediated RNA

655   decay by ER stress. RNA. 2017;23(3):378-94.

656   http://www.rnajournal.org/cgi/doi/10.1261/rna.058040.116

657   5.   Barberan-Soler S, Lambert NJ, Zahler AM. Global analysis of alternative splicing

658   uncovers developmental regulation of nonsense-mediated decay in C. elegans. RNA.

659   2009;15(9):1652-60. https://doi.org/10.1261/rna.1711109

660   6.   Bruno IG, Karam R, Huang L, Bhardwaj A, Lou CH, Shum EY, et al. Identification of a

661   microRNA that activates gene expression by repressing nonsense-mediated RNA decay. Mol

662   Cell. 2011;42(4):500-10. https://doi.org/10.1016/j.molcel.2011.04.018

663   7.   Gong C, Kim YK, Woeller CF, Tang Y, Maquat LE. SMD and NMD are competitive

664   pathways that contribute to myogenesis: effects on PAX3 and myogenin mRNAs. Genes Dev.

665   2009;23(1):54-66. http://www.genesdev.org/cgi/doi/10.1101/gad.1717309

666   8.   Usuki F, Yamashita A, Kashima I, Higuchi I, Osame M, Ohno S. Specific inhibition of

667   nonsense-mediated mRNA decay components, SMG-1 or Upf1, rescues the phenotype of

30

668   Ullrich disease fibroblasts. Mol Ther. 2006;14(3):351-60.

669   https://doi.org/10.1016/j.ymthe.2006.04.011

670   9.   Huang L, Shum EY, Jones SH, Lou CH, Dumdie J, Kim H, et al. A Upf3b-mutant mouse

671   model with behavioral and neurogenesis defects. Mol Psychiatry. 2018;23(8):1773-86.

672   https://doi.org/10.1038/mp.2017.173

673   10.   Karousis ED, Gypas F, Zavolan M, Muhlemann O. Nanopore sequencing reveals

674   endogenous NMD-targeted isoforms in human cells. Genome Biol. 2021;22(1):223.

675   https://doi.org/10.1186/s13059-021-02439-3

676   11.   Colombo M, Karousis ED, Bourquin J, Bruggmann R, Muhlemann O. Transcriptome-

677   wide identification of NMD-targeted human mRNAs reveals extensive redundancy between

678   SMG6- and SMG7-mediated degradation pathways. RNA. 2017;23(2):189-201.

679   http://www.rnajournal.org/cgi/doi/10.1261/rna.059055.116

680   12.   Pastor F, Kolonias D, Giangrande PH, Gilboa E. Induction of tumour immunity by

681   targeted inhibition of nonsense-mediated mRNA decay. Nature. 2010;465(7295):227-30.

682   https://doi.org/10.1038/nature08999

683   13.   Becker JP, Helm D, Rettel M, Stein F, Hernandez-Sanchez A, Urban K, et al. NMD

684   inhibition by 5-azacytidine augments presentation of immunogenic frameshift-derived

685   neoepitopes. iScience. 2021;24(4):102389. https://doi.org/10.1016/j.isci.2021.102389

686   14.   Tawil R, van der Maarel SM, Tapscott SJ. Facioscapulohumeral dystrophy: the path to

687   consensus on pathophysiology. Skelet Muscle. 2014;4:12. https://doi.org/10.1186/2044-5040-4-

688   12

689   15.   Hamel J, Tawil R. Facioscapulohumeral muscular dystrophy: update on pathogenesis

690   and future treatments. Neurotherapeutics. 2018;15(4):863-71. https://doi.org/10.1007/s13311-

691   018-00675-3

692   16.   De Iaco A, Planet E, Coluccio A, Verp S, Duc J, Trono D. DUX-family transcription

693   factors regulate zygotic genome activation in placental mammals. Nat Genet. 2017;49(6):941-5.

694   https://doi.org/10.1038/ng.3858

695   17.   Hendrickson PG, Dorais JA, Grow EJ, Whiddon JL, Lim JW, Wike CL, et al. Conserved

696   roles of mouse DUX and human DUX4 in activating cleavage-stage genes and MERVL/HERVL

697   retrotransposons. Nat Genet. 2017;49(6):925-34. https://doi.org/10.1038/ng.3844

698   18.   Whiddon JL, Langford AT, Wong CJ, Zhong JW, Tapscott SJ. Conservation and

699   innovation in the DUX4-family gene network. Nat Genet. 2017;49(6):935-40.

700   https://doi.org/10.1038/ng.3846

701   19.   Kowaljow V, Marcowycz A, Ansseau E, Conde CB, Sauvage S, Matteotti C, et al. The

702   DUX4 gene at the FSHD1A locus encodes a pro-apoptotic protein. Neuromuscul Disord.

703   2007;17(8):611-23. https://doi.org/10.1016/j.nmd.2007.04.002

704   20.   Bosnakovski D, Xu Z, Gang EJ, Galindo CL, Liu M, Simsek T, et al. An isogenetic

705   myoblast expression screen identifies DUX4-mediated FSHD-associated molecular pathologies.

706   EMBO J. 2008;27(20):2766-79. https://doi.org/10.1038/emboj.2008.201

707   21.   Wallace LM, Garwick SE, Mei W, Belayew A, Coppee F, Ladner KJ, et al. DUX4, a

708   candidate gene for facioscapulohumeral muscular dystrophy, causes p53-dependent myopathy

709   in vivo. Ann Neurol. 2011;69(3):540-52. https://doi.org/10.1002/ana.22275

710   22.   Rickard AM, Petek LM, Miller DG. Endogenous DUX4 expression in FSHD myotubes is

711   sufficient to cause cell death and disrupts RNA splicing and cell migration pathways. Hum Mol

712   Genet. 2015;24(20):5901-14. https://doi.org/10.1093/hmg/ddv315

713   23.   Feng Q, Snider L, Jagannathan S, Tawil R, van der Maarel SM, Tapscott SJ, et al. A

714   feedback loop between nonsense-mediated decay and the retrogene DUX4 in

715   facioscapulohumeral muscular dystrophy. Elife. 2015;4. https://doi.org/10.7554/eLife.04996

716   24.   Jagannathan S, Ogata Y, Gafken PR, Tapscott SJ, Bradley RK. Quantitative proteomics

717   reveals key roles for post-transcriptional gene regulation in the molecular pathology of

718   facioscapulohumeral muscular dystrophy. Elife. 2019;8. https://doi.org/10.7554/eLife.41740

719   25.   Yao Z, Snider L, Balog J, Lemmers RJ, Van Der Maarel SM, Tawil R, et al. DUX4-

720   induced gene expression is the major molecular signature in FSHD skeletal muscle. Hum Mol

721   Genet. 2014;23(20):5342-52. https://doi.org/10.1093/hmg/ddu251

722   26.   Jagannathan S, Shadle SC, Resnick R, Snider L, Tawil RN, van der Maarel SM, et al.

723   Model systems of DUX4 expression recapitulate the transcriptional profile of FSHD cells. Hum

724   Mol Genet. 2016;25(20):4419-31. https://doi.org/10.1093/hmg/ddw271

725   27.   Ingolia NT. Ribosome profiling: new views of translation, from single codons to genome

726   scale. Nat Rev Genet. 2014;15(3):205-13. https://doi.org/10.1038/nrg3645

727   28.   Geng LN, Yao Z, Snider L, Fong AP, Cech JN, Young JM, et al. DUX4 activates

728   germline genes, retroelements, and immune mediators: implications for facioscapulohumeral

729   dystrophy. Dev Cell. 2012;22(1):38-51. https://doi.org/10.1016/j.devcel.2011.11.013

730   29.   Shadle SC, Zhong JW, Campbell AE, Conerly ML, Jagannathan S, Wong CJ, et al.

731   DUX4-induced dsRNA and MYC mRNA stabilization activate apoptotic pathways in human cell

732   models of facioscapulohumeral dystrophy. PLoS Genet. 2017;13(3):e1006658.

733   https://doi.org/10.1371/journal.pgen.1006658

734   30.   Proud CG. eIF2 and the control of cell physiology. Semin Cell Dev Biol. 2005;16(1):3-12.

735   https://doi.org/10.1016/j.semcdb.2004.11.004

736   31.   Rendleman J, Mohammad MP, Pressler M, Maity S, Hronová V, Gao Z, et al. Regulatory

737   start-stop elements in 5' untranslated regions pervasively modulate translation. bioRxiv. 2021.

738   https://doi.org/10.1101/2021.07.26.453809

739   32.   Calviello L, Hirsekorn A, Ohler U. Quantification of translation uncovers the functions of

740   the alternative transcriptome. Nat Struct Mol Biol. 2020;27(8):717-25.

741   https://doi.org/10.1038/s41594-020-0450-4

742 33.   Anders S, Reyes A, Huber W. Detecting differential usage of exons from RNA-seq data.

743 Genome Res. 2012;22(10):2008-17. http://www.genome.org/cgi/doi/10.1101/gr.133744.111

744 34.   More DA, Kumar A. SRSF3: Newly discovered functions and roles in human health and

745 diseases. Eur J Cell Biol. 2020;99(6):151099. https://doi.org/10.1016/j.ejcb.2020.151099

746 35.   Zhou Z, Gong Q, Lin Z, Wang Y, Li M, Wang L, et al. Emerging roles of SRSF3 as a

747 therapeutic target for cancer. Front Oncol. 2020;10:577636.

748 https://doi.org/10.3389/fonc.2020.577636

749 36.   Kano S, Nishida K, Nishiyama C, Akaike Y, Kajita K, Kurokawa K, et al. Truncated

750 serine/arginine-rich splicing factor 3 accelerates cell growth through up-regulating c-Jun

751 expression. J Med Invest. 2013;60(3-4):228-35. https://doi.org/10.2152/jmi.60.228

752 37.   Kano S, Nishida K, Kurebe H, Nishiyama C, Kita K, Akaike Y, et al. Oxidative stress-

753 inducible truncated serine/arginine-rich splicing factor 3 regulates interleukin-8 production in

754 human colon cancer cells. Am J Physiol Cell Physiol. 2014;306(3):C250-62.

755 https://doi.org/10.1152/ajpcell.00091.2013

756 38.   Jimenez M, Urtasun R, Elizalde M, Azkona M, Latasa MU, Uriarte I, et al. Splicing

757 events in the control of genome integrity: role of SLU7 and truncated SRSF3 proteins. Nucleic

758 Acids Res. 2019;47(7):3450-66. https://doi.org/10.1093/nar/gkz014

759 39.   Langner HK, Jastrzebska K, Caruthers MH. Synthesis and characterization of

760 thiophosphoramidate morpholino oligonucleotides and chimeras. J Am Chem Soc.

761 2020;142(38):16240-53.https://doi.org/10.1021/jacs.0c04335

762 40.   Paul S, Caruthers MH. Synthesis of backbone modified morpholino oligonucletodies and

763 chimeras using phosphoramidite chemistry. 2022. U.S. Patent No. 11,230,565 B2.

764 41.   Kurosaki T, Maquat LE. Nonsense-mediated mRNA decay in humans at a glance. J Cell

765 Sci. 2016;129(3):461-7. https://doi.org/10.1242/jcs.181008

766   42.   Homma S, Beermann ML, Boyce FM, Miller JB. Expression of FSHD-related DUX4-FL

767   alters proteostasis and induces TDP-43 aggregation. Ann Clin Transl Neurol. 2015;2(2):151-66.

768   https://doi.org/10.1002/acn3.158

769   43.   Homma S, Beermann ML, Yu B, Boyce FM, Miller JB. Nuclear bodies reorganize during

770   myogenesis in vitro and are differentially disrupted by expression of FSHD-associated DUX4.

771   Skelet Muscle. 2016;6(1):42. https://doi.org/10.1186/s13395-016-0113-7

772   44.   Frisullo G, Frusciante R, Nociti V, Tasca G, Renna R, Iorio R, et al. CD8(+) T cells in

773   facioscapulohumeral muscular dystrophy patients with inflammatory features at muscle MRI. J

774   Clin Immunol. 2011;31(2):155-66. https://doi.org/10.1007/s10875-010-9474-6

775   45.   Arahata K, Ishihara T, Fukunaga H, Orimo S, Lee JH, Goto K, et al. Inflammatory

776   response in facioscapulohumeral muscular dystrophy (FSHD): immunocytochemical and

777   genetic analyses. Muscle Nerve Suppl. 1995;2:S56-66. https://doi.org/10.1002/mus.880181312

778   46.   Hauerslev S, Orngreen MC, Hertz JM, Vissing J, Krag TO. Muscle regeneration and

779   inflammation in patients with facioscapulohumeral muscular dystrophy. Acta Neurol Scand.

780   2013;128(3):194-201. https://doi.org/10.1111/ane.12109

781   47.   Tasca G, Pescatori M, Monforte M, Mirabella M, Iannaccone E, Frusciante R, et al.

782   Different molecular signatures in magnetic resonance imaging-staged facioscapulohumeral

783   muscular dystrophy muscles. PLoS One. 2012;7(6):e38779.

784   https://doi.org/10.1371/journal.pone.0038779

785   48.   Desai A, Hu Z, French CE, Lloyd JPB, Brenner SE. Networks of splice factor regulation

786   by unproductive splicing coupled with nonsense mediated mRNA decay. bioRxiv. 2020.

787   https://doi.org/10.1101/2020.05.20.107375

788   49.   Barger CJ, Branick C, Chee L, Karpf AR. Pan-cancer analyses reveal genomic features

789   of FOXM1 overexpression in cancer. Cancers (Basel). 2019;11(2).

790   https://doi.org/10.3390/cancers11020251

791   50.   Livak KJ, Schmittgen TD. Analysis of relative gene expression data using real-time

792   quantitative PCR and the 2(-Delta Delta C(T)) method. Methods. 2001;25(4):402-8.

793   https://doi.org/10.1006/meth.2001.1262

794   51.   Langmead B, Salzberg SL. Fast gapped-read alignment with Bowtie 2. Nat Methods.

795   2012;9(4):357-9. https://doi.org/10.1038/nmeth.1923

796   52.   Dobin A, Davis CA, Schlesinger F, Drenkow J, Zaleski C, Jha S, et al. STAR: ultrafast

797   universal RNA-seq aligner. Bioinformatics. 2013;29(1):15-21.

798   https://doi.org/10.1093/bioinformatics/bts635

799   53.   Calviello L, Sydow D, Harnett D, Ohler U. Ribo-seQC: comprehensive analysis of

800   cytoplasmic and organellar ribosome profiling data. bioRxiv. 2019.

801   https://doi.org/10.1101/601468

802   54.   Love MI, Huber W, Anders S. Moderated estimation of fold change and dispersion for

803   RNA-seq data with DESeq2. Genome Biol. 2014;15(12):550. https://doi.org/10.1186/s13059-

804   014-0550-8

805   55.   Liao Y, Smyth GK, Shi W. featureCounts: an efficient general purpose program for

806   assigning sequence reads to genomic features. Bioinformatics. 2014;30(7):923-30.

807   https://doi.org/10.1093/bioinformatics/btt656

808   56.   Zhu A, Ibrahim JG, Love MI. Heavy-tailed prior distributions for sequence count data:

809   removing the noise and preserving large differences. Bioinformatics. 2019;35(12):2084-92.

810   https://doi.org/10.1093/bioinformatics/bty895

811   57.   Calviello L, Venkataramanan S, Rogowski KJ, Wyler E, Wilkins K, Tejura M, et al. DDX3

812   depletion represses translation of mRNAs with complex 5' UTRs. Nucleic Acids Res.

813   2021;49(9):5336-50. https://doi.org/10.1093/nar/gkab287

814   58.   Chothani S, Adami E, Ouyang JF, Viswanathan S, Hubner N, Cook SA, et al. deltaTE:

815   Detection of translationally regulated genes by integrative analysis of Ribo-seq and RNA-seq

816   data. Curr Protoc Mol Biol. 2019;129(1):e108. https://doi.org/10.1002/cpmb.108

817   59.   Merrick WC, Hensold JO. Analysis of eukaryotic translation in purified and semipurified

818   systems. Curr Protoc Cell Biol. 2001;Chapter 11:Unit 11 9.

819   https://doi.org/10.1002/0471143030.cb1109s08

820   60.   Miura P, Andrews M, Holcik M, Jasmin BJ. IRES-mediated translation of utrophin A is

821   enhanced by glucocorticoid treatment in skeletal muscle cells. PLoS One. 2008;3(6):e2309.

822   https://doi.org/10.1371/journal.pone.0002309

823   61.   Schneider CA, Rasband WS, Eliceiri KW. NIH Image to ImageJ: 25 years of image

824   analysis. Nat Methods. 2012;9(7):671-5. https://doi.org/10.1038/nmeth.2089

825   62.   Huber W, Carey VJ, Gentleman R, Anders S, Carlson M, Carvalho BS, et al.

826   Orchestrating high-throughput genomic analysis with Bioconductor. Nat Methods.

827   2015;12(2):115-21. https://doi.org/10.1038/nmeth.3252

828   63.   Wickham H. ggplot2: Elegant graphics for data analysis. New York, NY: Springer-Verlag;

829   2016.

830   64.   Shadle SC, Bennett SR, Wong CJ, Karreman NA, Campbell AE, van der Maarel SM, et

831   al. DUX4-induced bidirectional HSATII satellite repeat transcripts form intranuclear double-

832   stranded RNA foci in human cell models of FSHD. Hum Mol Genet. 2019;28(23):3997-4011.

833   https://doi.org/10.1093/hmg/ddz242

834

835 **APPENDIX**

836

837 **KEY RESOURCES TABLE**

Reagent type (species) or resource	Designation	Source or reference	Identifiers	Additional information
cell line (*Homo sapiens*)	293T	ATCC	CRL-3216, RRID:CVCL_0063	
cell line (*H. sapiens*)	MB135	Stephen Tapscott		Female control myoblast line
cell line (*H. sapiens*)	MB135-iDUX4	[26]		Harbors doxycycline-inducible DUX4 transgene
cell line (*H. sapiens*)	MB135-iDUX4/ZSCAN4-mCherry	Stephen Tapscott		Harbors doxycycline-inducible DUX4 transgene and DUX4-responsive fluorescent reporter
cell line (*H. sapiens*)	MB135-iFLAG-SRSF3-FL	This paper		Harbors doxycycline-inducible, FLAG-tagged, codon-optimized, full-length SRSF3
cell line (*H. sapiens*)	MB135-iFLAG-SRSF3-TR	This paper		Harbors doxycycline-inducible, FLAG-tagged, codon-optimized, truncated SRSF3
cell line (*H. sapiens*)	MB200	Stephen Tapscott		Male FSHD myoblast line
antibody	anti-DUX4 (Rabbit monoclonal)	Abcam	ab124699, RRID:AB_10973363	IF(1:200), WB(1:1000)
antibody	anti-Histone H3 (Rabbit polyclonal)	Abcam	ab1791, RRID:AB_302613	WB(1:5000)
antibody	anti-SRSF3 (Mouse monoclonal)	Thermo Fisher Scientific	33-4200, RRID:AB_2533119	WB(1:250)
antibody	anti-SRSF3-TR (Rabbit polyclonal)	This paper		IF(1:200), WB(1:500)
antibody	anti-RENT1/hUPF1 (Rabbit monoclonal)	Abcam	ab109363, RRID:AB_10861979	WB(1:1000)
recombinant DNA reagent	pCW57.1-FLAG-SRSF3_Full.Length_Codon.Optimized-Blast (plasmid)	This paper		All-in-one lentiviral vector for doxycycline-inducible expression of FLAG-

38

				tagged, codon-optimized, full-length SRSF3
recombinant DNA reagent	pCW57.1-FLAG-SRSF3_Truncated_Codon.Optimized-Blast (plasmid)	This paper		All-in-one lentiviral vector for doxycycline-inducible expression of FLAG-tagged, codon-optimized, truncated SRSF3
recombinant DNA reagent	pCW57-MCS1-P2A-MCS2 (Blast) (plasmid)	Addgene	Plasmid #80921, RRID:Addgene_80921	
recombinant DNA reagent	pMD2.G (plasmid)	Addgene	Plasmid #12259; RRID:Addgene_12259	
recombinant DNA reagent	psPAX2 (plasmid)	Addgene	Plasmid #12260; RRID:Addgene_12260	
recombinant DNA reagent	pTwist-FLAG-SRSF3_Full.Length_Codon.Optimized (plasmid)	This paper		For expression of FLAG-tagged, codon-optimized full-length SRSF3 in mammalian cells; synthesized by Twist Bioscience
recombinant DNA reagent	pTwist-FLAG-SRSF3_Truncated_Codon.Optimized (plasmid)	This paper		For expression of FLAG-tagged, codon-optimized truncated SRSF3 in mammalian cells; synthesized by Twist Bioscience
sequence-based reagent	DUX4 transgene F	[64]	qPCR primers	TAGGGGAAGAGGTAGACGGC
sequence-based reagent	DUX4 transgene R	[64]	qPCR primers	CGGTTCCGGGATTCCGATAG
sequence-based reagent	KHDC1L F	[26]	qPCR primers	CACCAATGGCAAAGCAGTGG
sequence-based reagent	KHDC1L R	[26]	qPCR primers	TCAGTCTCCGGTGTACGGTG
sequence-based reagent	SRSF3 F	[23]	qPCR primers	TGGAACTGTCGAATGGTGAA
sequence-based reagent	SRSF3 NMD- R	[23]	qPCR primers	CTTGGAGATCTGCGACGAG

sequence-based reagent	SRSF3 NMD+ R	[23]	qPCR primers	GGGTGGTGAGAAGAGACATGA
sequence-based reagent	SRSF3_TMO-11	This paper	antisense oligonucleotide	G*A*T*G*G*t*g*a*c*t*c*t*g*c*g*A*C*G*A*g (*, thiophosphoramidate or thiophosphate internucleotide linkage; capital letter, morpholino nucleoside; lowercase letter, 2'deoxynucleoside)
sequence-based reagent	RPL27 F	[26]	qPCR primers	GCAAGAAGAAGATCGCCAAG
sequence-based reagent	RPL27 R	[26]	qPCR primers	TCCAAGGGGATATCCACAGA
peptide, recombinant protein	Insulin-Transferrin-Selenium	Thermo Fisher Scientific	41400045	
peptide, recombinant protein	Protein G Sepharose	Thermo Fisher Scientific	101241	
peptide, recombinant protein	Recombinant human basic fibroblast growth factor	Promega	G5071	
chemical compound, drug	Blasticidin S HCl	Thermo Fisher Scientific	R21001	
chemical compound, drug	Cycloheximide	Sigma-Aldrich	239765	
chemical compound, drug	Doxycycline hyclate	Sigma-Aldrich	D9891	
chemical compound, drug	Lipofectamine 2000 Transfection Reagent	Thermo Fisher Scientific	11668-030	
chemical compound, drug	Lipofectamine RNAiMAX Transfection Reagent	Thermo Fisher Scientific	13778-150	
chemical compound, drug	MG132	Sigma-Aldrich	474790	

chemical compound, drug	Puromycin dihydrochloride	VWR	97064-280	
chemical compound, drug	TRIzol Reagent	Thermo Fisher Scientific	15596018	
commerical assay or kit	BCA Protein Assay Kit	Pierce	23225	
commerical assay or kit	Caspase-Glo 3/7 Assay System	Promega	G8091	
commerical assay or kit	Direct-zol RNA Miniprep Kit	Zymo Research	R2051	
commerical assay or kit	NEXTflex Rapid Directional qRNA-Seq Kit	Bioo Scientific	NOVA-5130-02D	
commerical assay or kit	NEXTflex Small RNA-Seq Kit v3	Bioo Scientific	NOVA-5132-06	
commerical assay or kit	Ribo-Zero rRNA Removal Kit	Illumina	MRZH11124, discontinued	
commerical assay or kit	SuperScript III First-Strand Synthesis System	Thermo Fisher Scientific	18080051	
software, algorithm	Code used for RNA-seq and Ribo-seq figure generation	This paper		The code used for the RNA-seq and Ribo-seq figure generation can be accessed via github at https://github.com/sjaganna/2021-campbell_dyle_calviello_et_al
software, algorithm	GraphPad Prism	GraphPad Prism (https://graphpad.com)	RRID:SCR_002798	Version 9
software, algorithm	ImageJ	ImageJ (https://imagej.nih.gov)	RRID:SCR_003070	